Intrinsic spatial chirp of subcycle terahertz pulsed beams

G. A. Hine and M. Doleans

Phys. Rev. A **104**, 032229 — Published 30 September 2021

DOI: 10.1103/PhysRevA.104.032229

Intrinsic Spatial Chirp of Subcycle Terahertz Pulsed Beams

G. A. Hine* and M. Doleans
Oak Ridge National Laboratory
(Dated: September 15, 2021)

We present an analysis of spatial chirp in subcycle pulsed beams corroborated by spatio-temporal electro-optic sampling measurements of terahertz radiation. Modeling the subcycle pulsed beam as a superposition of monochromatic Gaussian beams, free-space propagation is shown to directly lead to lateral spatial chirp, with the spectrum on-axis substantially bluer than the overall energy spectrum. The 2-transverse + 1-temporal dimensional profile of terahertz subcycle pulsed beams from organic crystals DSTMS and OH1 are measured and compared, with observed spatio-spectral correlations consistent with the model.

I. INTRODUCTION

Since the advent of chirped-pulse amplification[1] and optical parametric chirped-pulse amplification[2], accessible laser intensities have been steadily increasing[3]. With these techniques, comparatively compact systems can leverage temporal compression of laser energy to achieve high peak power, enabling wider access to intense lasers and facilitating development of applications in a broad range of scientific and technological fields as sources of energetic particles[4–6], coherent ultraviolet and x-rays[7, 8], and unprecedented bright sources of terahertz (THz) radiation[9]. Bright THz sources, utilizing various techniques such as two-color mixing in plasmas[10, 11], bulk and surface optical rectification in nonlinear crystals[12–14], or through laser interaction with a thin liquid[15] or solid target[16], have in turn enabled new research, for example in materials science[17], impact ionization and electron emission[18, 19], or for novel concepts for particle accelerators and undulators[20–23]. Strong THz fields are achieved through the conjunction of high pulse energy and high beam quality. Though the former can straightforwardly be measured using bolometers or pyroelectric sensors, the latter is harder to quantify in particular because of the broadband nature of ultrashort THz sources[24] and spatio-temporal coupling which will be shown to emerge here.

While the ultrashort pump pulses used to generate the THz in various methods can be considered broadband, often the relative bandwidth of the THz itself is significantly larger. For example, the THz radiation generated by optical rectification of femtosecond laser pulses in organic crystals is extremely broadband, spanning several octaves[25]. Such radiation can be considered subcycle (SC) because the pulse duration is of the same order as the period of oscillation. With increasing interest in further compression of infrared lasers for high-intensity applications ([6] for example), SC THz can be seen as a surrogate system in which to study the behaviour optical pulses in the limit of compression, and inform on ultrabroadband wave phenomena. For example, in this regime, the slowly varying envelope approximation has been shown to break down, and the pulse exhibits an intrinsic chirp with the lower frequencies being less temporally localized than the higher[26]. The spectrum of a SC THz pulse was later shown to blue shift upon propagation through the focal region[27]. While under linear propagation, the overall energy spectrum of a wave should be conserved, the spectra in [27] corresponded to the temporal evolution of the THz fields at a single transverse spatial coordinate (or more precisely, averaged over a small transverse area). Consequently, in such 1D measurements, geometrical focusing effects can change the observed spectrum as the various frequency components redistribute throughout the focal volume.

In deference to this, we will make a distinction between beams, pulses, and pulsed beams. A travelling wave which is confined in its transverse dimensions and propagates in free space or a uniform medium is referred to as a beam. A travelling wave which is confined in its temporal coordinate (eg. t or $\xi = z - vt$) is referred to as a pulse, and may be used to describe the temporal evolution of a wave at a point, averaged over a finite area, or integrated over all transverse space. Finally, a wave which is simultaneously confined transversely and temporally is referred to as a pulsed beam.

II. MODELING SUBCYCLE PULSED BEAMS

We will now investigate the propagation of the subcycle pulsed beam (SCPB) at THz frequencies, and the spatio-temporal and spatio-spectral correlations that emerge, first introducing a model for describing spatio-spectral behavior and then comparing it with measurements of THz SCPBs using a 2-transverse + 1-temporal dimensional (2+1D) version of electro-optic sampling. Anticipating the breakdown of the carrier-envelope approximation, we represent the SCPB as a superposition of monochromatic paraxial Gaussian beams. We will initially consider an SCPB for which the component beams share a common beam waist w_0, and all have flat phase fronts at a longitudinal position $z = 0$. For an arbitrary, complex amplitude spectrum $\widetilde{A}_0(f)$, the electric field can

* hinega@ornl.gov

be expressed as,

$$\psi(x,y,z=0,t) = 2\Re\left(\int_0^\infty df e^{i2\pi ft}\frac{\sqrt{2/\pi}}{w_0}e^{-\frac{x^2+y^2}{w_0^2}}\tilde{A}_0(f)\right) \quad (1)$$

which is constructed such that $\left|\tilde{A}_0(f)\right|^2$ gives the overall energy spectrum of the SCPB. At this longitudinal position, the transverse dependence of the pulse is separable from the spectral dependence, which is a property of this construction, and is not universal. For example, the SCPB in [28] was constructed such that all frequencies shared the same Rayliegh range, and at no longitudinal position could it be described by Eq. (1). When the independent propagation at each frequency is included in Eq. (1), the transverse dependence couples with the frequency through z to produce a correlated *spatio-spectrum* $\tilde{A}(x,y,z,f)$.

Including propagation of the independent component gaussian beams, we can construct the full spatio-temporal pulse profile $\psi(x,y,z,t)$ from $\tilde{A}_0(f)$.

$$\psi(x,y,z,t) = 2\Re\left(\int_0^\infty df e^{i2\pi ft}\tilde{A}(x,y,z,f)\right) \quad (2)$$

$$\tilde{A}(x,y,z,f) = \tilde{A}_0(f)\frac{\sqrt{2/\pi}}{w_0\sqrt{1+z^2/z_R^2(f)}} \times e^{i\Phi(z,f)}e^{-\frac{x^2+y^2}{w^2(z,f)}}e^{i2\pi fn(f)\frac{x^2+y^2}{2R(z,f)}} \quad (3)$$

Here, we have allowed for frequency dependence of the Gouy phase $\Phi(z,f) = \arctan(z/z_0(f))$, the phase front radius of curvature $R(z,f) = z + z_R^2(f)/z$, the beam width $w(z,f) = w_0\sqrt{1+z^2/z_R^2(f)}$, and the Rayleigh range $z_R(f) = \pi w_0^2 fn(f)/c$ with $c/n(f)$ the phase velocity at frequency f.

Since the Rayleigh range and beam waist cannot simultaneously be made independent of frequency, no gaussian pulse of finite bandwidth can maintain perfect transverse spectral uniformity, with an exception for the case where the refractive index $n(f) \propto 1/f$ for all relavent frequencies. We observe the far-field spatio-spectrum,

$$\tilde{A}(x,y,z\gg z_R,f) = i\frac{\sqrt{2/\pi}}{w_0}\frac{z_R(f)}{z}e^{i2\pi\frac{x^2+y^2}{2zc/fn(f)}}e^{-\frac{x^2+y^2}{(w_0z/z_R(f))^2}}\tilde{A}_0(f) \quad (4)$$

wherein the component beams have become spatially separated with width and divergence inversely proportional to frequency. We also see that on-axis ($x=y=0$) the spectrum is blue-shifted, while in the periphery, redder frequencies dominate.

Similarly, we can look at the SCPB when focused. We will assume focusing with a numerical aperture NA independent of frequency, which is consistent with the use of a focusing optic without chromatic aberration such as a reflective paraboloid. In the paraxial approximation in vacuum, the Gaussian beam waist is related to the frequency by $w_0 = 2\pi c/f\text{NA}$, and we can construct the focus spatio-spectrum $\tilde{A}(x,y,z=0,f)$ directly from $\tilde{A}_0$, maintaining the overall energy spectrum.

$$\tilde{A}(x,y,z=0,f) = \frac{\sqrt{2/\pi}}{2\pi c/f\text{NA}}e^{-\frac{x^2+y^2}{(2\pi c/f\text{NA})^2}}\tilde{A}_0(f) \quad (5)$$

This results in similar dependencies to that of the far-field spatio-spectrum, but without phase front curvature on the component beams. The higher frequencies experience greater transverse confinement than the lower, broadening and blue-shifting the on-axis spectrum, while spectra toward the periphery are narrower and redder.

Figure 1 shows a plot of such a spatio-spectrum with frequencies and transverse sizes chosen to represent a focused single-cycle THz pulse. Here, we have adapted the functional form of the amplitude spectrum from [28], $A_0(f) = N_c(f/f_0)^s e^{-\frac{sf}{f_0}}$ with normalization constant N_c. We chose the frequency scale $f_0 = 0.7$ THz and the order $s = 2$ to represent spectra generated by optical rectification in OH1[25, 29]. The resulting spatio-spectrum is horn-shaped and is substantially bluer than $\tilde{A}_0(f)$ on-

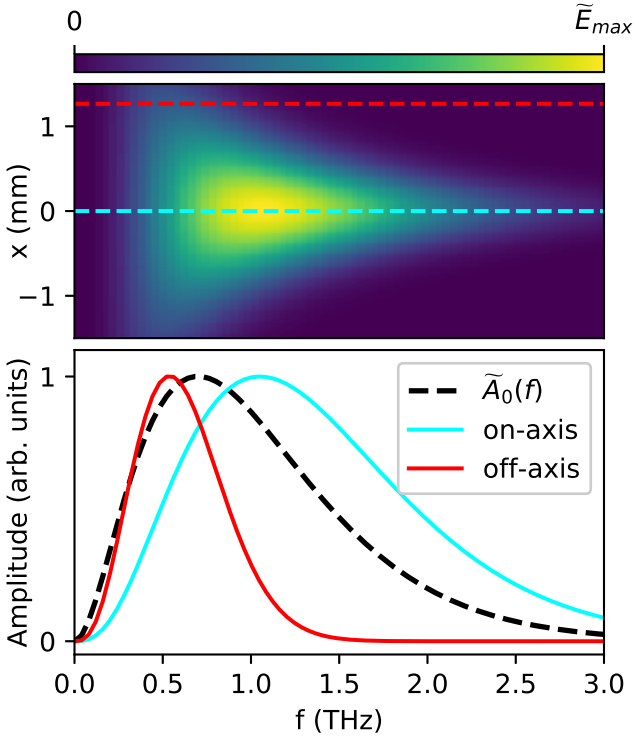

FIG. 1. Spectral redistribution upon focusing. (Top) The amplitude spatio-spectrum of a Gaussian SCPB focused with constant NA. Beam waist inversely proportional to frequency leads to a horn-shaped spatio-spectrum. (Bottom) When compared to $A_0(f)$ (black dashed curve), the local spectrum is shifted blue on-axis (cyan (light gray) solid curve) and red off-axis (red (dark gray) solid curve).

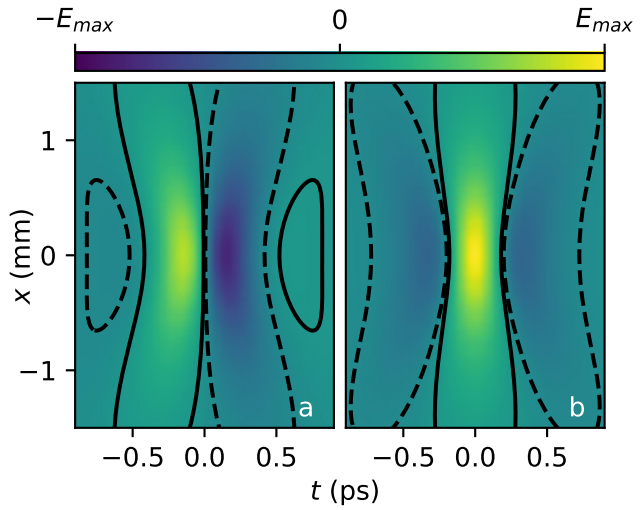

FIG. 2. Theoretical spatio-temporal profile of a SCPB. The superposition of Gaussian beams according to the spectrum in FIG. 1 produces (a) sine- and (b) cosine-like SCPBs for absolute phase π and 0 respectively. Black contours at 5% and −5% of the maximum field magnitude are overlaid to visualize the change in period with transverse coordinate x. The period is shortest on-axis at the peak of the pulse and increases in the transverse periphery, where it both precedes the on-axis pulse and persists after it has passed.

axis and redder in the periphery.

We use this spectrum to construct the spatio-temporal pulse profile according to Eq. (2). The resulting sine- and cosine-like pulses are shown in FIG. 2 with solid and dashed black contours at 5% and −5% of the peak field magnitude respectively. Wavefronts in the transverse periphery flare out earlier and later in time, resembling a piece of farfalle. It should be noted that although the wavefronts exhibit an instantaneous curvature, they have arisen from the superposition of aberration-free monochromatic beams sharing the same focal geometry. Because of this, we call the resulting spatial chirp intrinsic, representing a natural property of pulsed beams and not resulting from aberrations induced by optical elements.

III. MEASURING TERAHERTZ SUBCYCLE PULSED BEAMS

In order to observe this intrinsic spatial chirp in a THz SCPB, we developed a 2+1D electro-optic sampling method which preserves spatio-temporal correlations. Electro-optic sampling (EOS) is an extremely powerful technique which provides a coherent measurement of the electric field of a THz pulse. The THz electric field acts as a quasi-static external field in an electro-optic medium, inducing birefringence by Pockels effect. For a sufficiently short probe pulse (shorter than the THz period), this birefringence can be measured and the THz field reconstructed by observing changes in the probe as a function of delay.

Most commonly, the polarization state of the probe is ascertained using a Wollaston prism and a balanced photodetecter (BPD). However, the BPD averages over the transverse area of the probe which samples only a small region within the THz transverse profile. A conjugate measurement of the THz transverse profile can be made, for example, with an uncooled microbolometer focal plane array[25, 30], but the combination of these techniques does not capture spatio-temporal correlations like the phase-front flaring seen in FIG. 2. Imaging utilizing Pockels effect at a fixed time has been demonstrated, though it was not used for a full 2+1D measurement[31]. Some 1-transverse + 1-temporal dimensional single-shot measurements have been demonstrated[32, 33], but the ultrabroadband focus behavior described here was not observed. Finally, a temporally scanned transverse interferometric technique has been demonstrated[34], but again, spatio-spectral correlations at the focus were not reported.

For our 2+1D EOS measurement, we replace the Wollaston prism and balanced photodetector of a typical 1D EOS measurement (described in [35] or [36] for example) with a polarizing optic and a CCD. A 4f imaging system facilitates reconstructing the probe from the exit of the electrooptic medium onto the CCD. With an ultrashort probe transversely larger than the THz spot size, the THz electric field induces a *local* change in the probe polarization. This change in polarization, after imaging through the polarizer, manifests as a change in fluence on the CCD, with local electric field of positive (negative) polarity causing a local increase (decrease) in fluence.

Figure 3 shows a schematic of the experimental setup. THz SCPBs were generated by co-linear optical rectification in OH1 and DSTMS[29] (Rainbow Photonics AG). The OH1 (DSTMS) was pumped with 1300 nm (1450 nm) output of a LightConversion TOPAS tunable OPA pumped by a kHz repetition rate Ti:Sapphire laser (Coherent Astrella 30 fs 4.3 mJ) and had 0.4 mJ (0.34 mJ) of energy. The pump profile (FIG. 4) is supergaussian of order 1.5 and slightly overfills the clear aperture of the DSTMS and OH1. This aperture is visualized as a pupil overlaid on the profile. A fit to a supergaussian is shown in FIG. 4(b) with dashed lines again indicating the clear aperture of the organic crystal mounts. The generated THz radiation was initially focused at an f-number ($f/\# \approx (2\mathrm{NA})^{-1}$) of $f/8.5$ by a RFL = 1 off-axis parabola and the focus relayed by a pair of parabolic mirrors with 3x demagnification to a GaP crystal, resulting in final focusing with $f/2.9$. A vertically polarized probe, picked off from the Ti:Sapphire beam line before the OPA, was focused with $f/17$ through a 3 mm drilled hole in the last parabolic mirror, and diverged to a radius (e^{-2} of peak fluence) of 2.8 mm at the GaP.

The probe polarization input to the GaP was linear and oriented vertically. In the imaging system following the GaP, the probe encounters a $\frac{1}{4}\lambda$ wave plate oriented

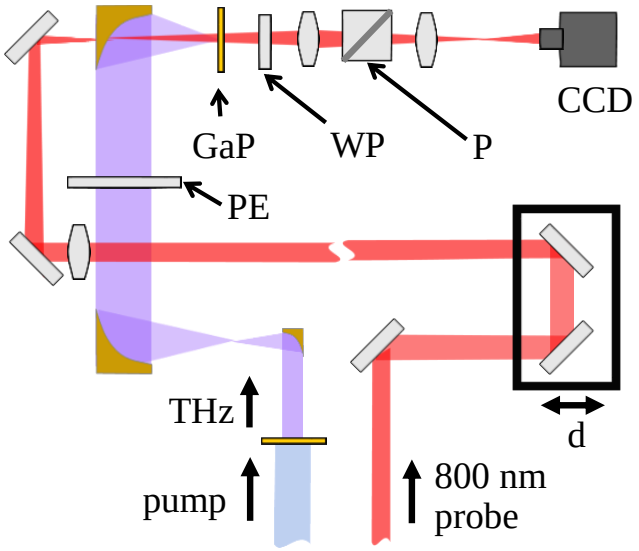

FIG. 3. Experimental Setup. A 1450 nm (1300 nm) pump generates a THz SCPB by optical rectification in DSTMS (OH1). The THz is relayed through a polyethylene filter (PE) and focused into the electro-optic medium (GaP). An 800 nm 30 fs probe passes through a variable delay line (d) and is focused through a 3 mm drilled hole in the final focusing mirror, expanding to over twice the transverse size of the THz SCPB as they copropagate in the GaP. The probe is imaged to a CCD through a quarter-wave plate (WP) and a polarizer (P), with local changes in polarization causing changes in fluence on the CCD.

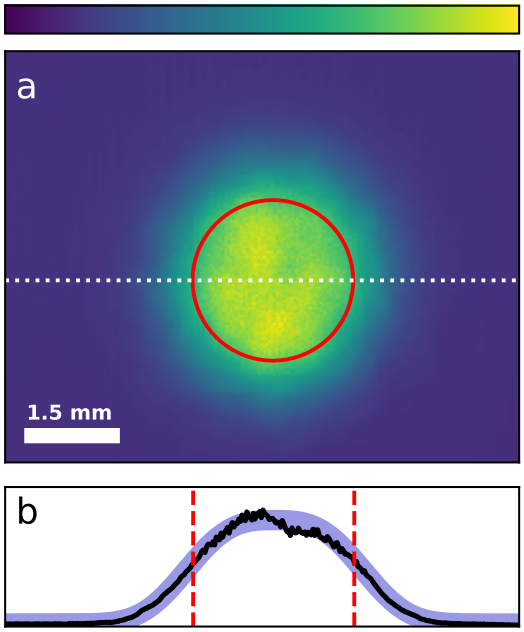

FIG. 4. Pump Profile. (a) Pump profile incident on organic crystals OH1 and DSTMS with clear aperture of the crystal mount indicated with a 3 mm diameter red pupil. The colorbar ranges from 0 to the maximum fluence. (b) A horizontal line-out of the pump profile at the vertical location indicated by the dotted line in (a), overlaid on a super-Gaussian profile of order 1.5 with good agreement. Vertical dashed red lines indicate the clear aperture of the crystal mount.

at 45° to the horizontal, and a beamsplitter transmitting only horizontal polarization to the CCD. The total fluence on the CCD $V(\Gamma)$ as function of the retardation Γ can be calculated by sequentially applying Jones matrices for each optical element to the input linear polarization E_i.

$$V(\Gamma) \propto |P_x Q T(\Gamma) E_i|^2 = E_0^2 \left(1 + \sin\Gamma/2 \cos\Gamma/2\right) \quad (6)$$

Here, $T(\Gamma)$ is the Jones matrix for a variable retarder oriented at 45° WRT the horizontal and represents the elctro-optic medium under the influence of the THz, Q for a quarter-wave plate also oriented at 45°, and P_x for a polarizer selecting horizontal polarization. Without knowing the constant of proportionality, we can use a reference image V_0, for which the THz is blocked to recover the retardation from the CCD signal,

$$\sin\Gamma \cos\Gamma = 2(V(\Gamma)/V_0 - 1) \approx \Gamma \quad (7)$$

In the limit of small retardation, $\Gamma(x, y)$ is related to the transverse electric field $E_x(x, y)$ by a material-specific proportionality constant[35, 36]. The spatio-temporal profile $E_x(x, y, t)$ was assembled by stacking measurements of $E_x(x, y)$ over a range of delays. Figure 5 shows the extracted THz electric field generated in OH1 and DSTMS as seen through y-t (FIG. 5(a,c)) and x-t (FIG. 5(b,d)) slices of the full 2+1D measurement. Plots of the temporal field evolution at two transverse positions are compared in FIG. 5(e). The measured pulsed beam exhibits spatial chirp like that seen in the model, with the temporal evolution of the field on-axis shorter, bluer, and arriving later than that off-axis.

The corresponding spatio-spectra of FIG. 5(b,c) were calculated by FFT along the temporal dimension and are shown in FIG. 5(f,g). Higher frequencies are seen to focus to a smaller transverse size. White dotted curves representing a surface proportional to $1/f$ indicate good agreement with the constant NA focus model (FIG. 1). Although the DSTMS spectrum is significantly bluer than the OH1 spectrum, since the spatio-spectra in FIG. 5(f,g) share the same focusing geometry, they are confined by the same spatio-spectral horn.

IV. DISCUSSION

Although correlated spatio-spectral structure complicates the application of ultrabroadband pulsed beams, they are not always detrimental. For example, if uncorellated THz is imaged from its source to the target,

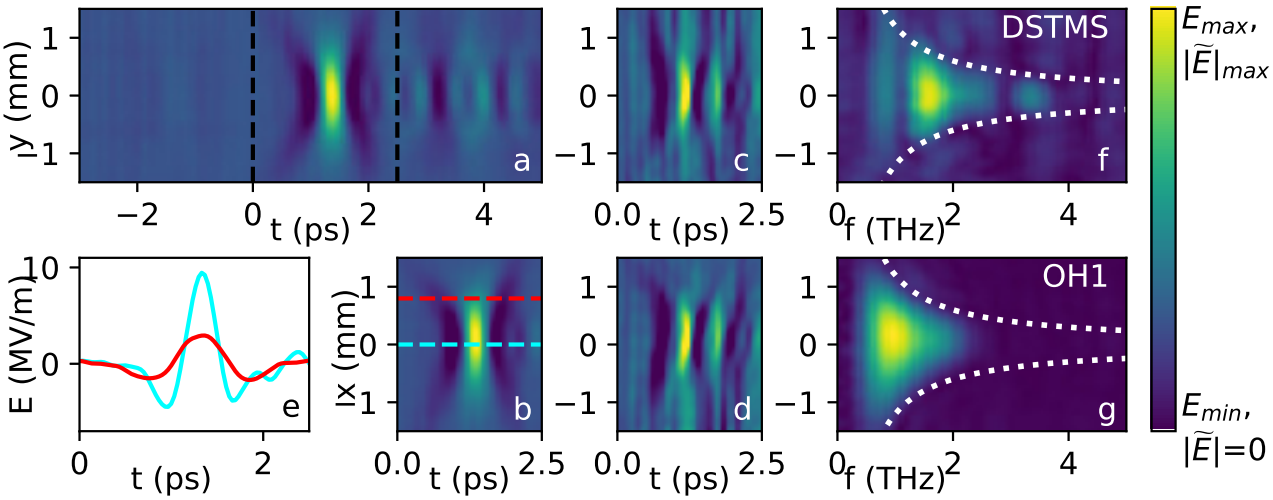

FIG. 5. Spatiotemporal measurement of THz SCPBs. THz electric fields from OH1 (a,b) and DSTMS (c,d) as seen in x-t (b,d) and y-t (a,c) slices through the center. The full temporal window in (a) shows the noise floor before the THz arrival followed by trailing oscillations from resonances in air and the crystals. Black dashed lines indicate the temporal window used for panels (b-g). The wavefronts can be seen to flare out towards the pulse periphery as seen in FIG. 2. The pulse on-axis, indicated by the cyan (light gray) dashed line in (b), is shown in panel (e) in cyan (light gray). In contrast, at 0.8 mm off-axis (indicated by the red (dark gray) dashed line in (b)), the pulse exhibits a longer period and duration, and arrives sooner (red (dark gray) in (e)). Spatio-spectra in (f) and (g) were computed from the SCPBs in (c) and (b) respectively, showing horn-shaped spatio-spectral correlations as in Fig. 1. The two spatio-spectra fit within the same $1/f$-horn indicated by white dotted curves, owing to the shared focusing geometry.

it will recover its initially uncorrelated structure. This is often the case, as for say, [37], wherein simulations were consistent with experimental results. However, as such a design is scaled up, any changes like using larger area sources[29], or a different focusing geometry, would render this no longer the case. Since fine-tuned pulse arrival time in each of the channels is central to the device operation, the variation in arrival time seen in FIG. 2 or FIG. 5 would be detrimental.

Beyond applications of bright THz, the motion of a free particle in a SCPB, already nontrivial in the relativistic case[4, 38, 39], would be further complicated because the driving field frequency and phase (not only amplitude) will change throughout the particles excursion. This behavior could be captured, say, in a particle tracking or particle-in-cell simulation. However, the normative form of a pulse typically follows the carrier-envelope approximation, especially in more sophisticated simulation frameworks[6, 39, 40]. While EM field solvers will naturally account for the independent behavior of different frequencies, an explicit definition of the SCPBs functional form is needed since the near field and far field cannot simultaneously be spectrally uniform. For example, when simulating the behavior of a SCPB, it could be specified which beam parameters (w_0, NA, z_R, etc.), if any, are uniform across the spectrum.

The transverse spatio-spectral correlations identified here are a conjugate representation of longitudinal spatio-spectral correlations seen in [25, 27], which manifested as spectral shifts throughout propagation. We argue that the 2+1D spatio-temporal measurement is a complete measure of a THz SCPB in that the field dependence on the longitudinal propagation coordinate follows from 2+1D form by the wave equation. This can be extended to the fully vectorial case in the paraxial approximation in vacuum or well-characterized media. For applications with Maxwell solvers, SCPBs of arbitrary spatio-spectral forms can be injected at the boundary of a simulation, and in that case the 2+1D EOS technique presented here could be used to define accurate input conditions. This would be especially useful if the spatio-spectrum of an available SCPB has a complex structure.

In summary, subcycle optical pulsed beams contain an intrinsic spatial chirp which manifests as lateral chirp upon propagation, even if lateral chirp is initially absent. A focused subcycle pulsed beam which is aberration free and free of spatial chirp exhibits time-dependent wavefront curvature at the focal plane. This was observed experimentally in coherent measurements of subcycle THz pulsed beams using a new 2-transverse + 1-temporal dimensional electro-optic sampling method. We recognize that this intrinsic spatial chirp result is not limited to THz frequencies but also applies to visible and mid-infrared supercontinuum, focusing of high harmonics, RF electromagnetic pulses, and to some extent to all coherent beams of finite spectral bandwidth.

ACKNOWLEDGMENTS

This manuscript has been authored by UT-Battelle, LLC under Contract No. DE-AC05-00OR22725 with the U.S. Department of Energy. This research used resources at the Spallation Neutron Source, a DOE Office of Science User Facility operated by the Oak Ridge National Laboratory.

This manuscript has been authored [optional: in part] by UT-Battelle, LLC, under contract DE-AC05-00OR22725 with the US Department of Energy (DOE). The US government retains and the publisher, by accepting the article for publication, acknowledges that the US government retains a nonexclusive, paid-up, irrevocable, worldwide license to publish or reproduce the published form of this manuscript, or allow others to do so, for US government purposes. DOE will provide public access to these results of federally sponsored research in accordance with the DOE Public Access Plan [41].

[1] D. Strickland and G. Mourou, Compression of amplified chirped optical pulses, Optics Communications **55**, 447 (1985).

[2] A. Dubietis, G. Jonuauskas, and A. Piskarskas, Powerful femtosecond pulse generation by chirped and stretched pulse parametric amplification in bbo crystal, Optics Communications **88**, 437 (1992).

[3] C. N. Danson, C. Haefner, J. Bromage, T. Butcher, J.-C. F. Chanteloup, E. A. Chowdhury, A. Galvanauskas, L. A. Gizzi, J. Hein, D. I. Hillier, and et al., Petawatt and exawatt class lasers worldwide, High Power Laser Science and Engineering **7**, e54 (2019).

[4] T. Tajima and J. M. Dawson, Laser electron accelerator, Phys. Rev. Lett. **43**, 267 (1979).

[5] A. J. Goers, G. A. Hine, L. Feder, B. Miao, F. Salehi, J. K. Wahlstrand, and H. M. Milchberg, Multi-mev electron acceleration by subterawatt laser pulses, Phys. Rev. Lett. **115**, 194802 (2015).

[6] F. Salehi, M. Le, L. Railing, M. Kolesik, and H. M. Milchberg, Laser-accelerated, low-divergence 15-mev quasimonoenergetic electron bunches at 1 khz, Phys. Rev. X **11**, 021055 (2021).

[7] M. Lewenstein, P. Balcou, M. Y. Ivanov, A. L'Huillier, and P. B. Corkum, Theory of high-harmonic generation by low-frequency laser fields, Phys. Rev. A **49**, 2117 (1994).

[8] C. Hernández-García, A. Jaron-Becker, D. D. Hickstein, A. Becker, and C. G. Durfee, High-order-harmonic generation driven by pulses with angular spatial chirp, Phys. Rev. A **93**, 023825 (2016).

[9] J. A. Flp, S. Tzortzakis, and T. Kampfrath, Laser-driven strong-field terahertz sources, Advanced Optical Materials **8**, 1900681 (2020).

[10] V. Y. Fedorov and S. Tzortzakis, Powerful terahertz waves from long-wavelength infrared laser filaments, Light: Science & Applications **9**, 1 (2020).

[11] K.-Y. Kim, A. Taylor, J. Glownia, and G. Rodriguez, Coherent control of terahertz supercontinuum generation in ultrafast laser–gas interactions, Nature photonics **2**, 605 (2008).

[12] W. Jia, M. Liu, Y. Lu, X. Feng, Q. Wang, X. Zhang, Y. Ni, F. Hu, M. Gong, X. Xu, *et al.*, Broadband terahertz wave generation from an epsilon-near-zero material, Light: Science & Applications **10**, 1 (2021).

[13] F. Lemery, T. Vinatier, F. Mayet, R. Aßmann, E. Baynard, J. Demailly, U. Dorda, B. Lucas, A.-K. Pandey, and M. Pittman, Highly scalable multicycle thz production with a homemade periodically poled macrocrystal, Communications Physics **3**, 1 (2020).

[14] X.-j. Wu, J.-l. Ma, B.-l. Zhang, S.-s. Chai, Z.-j. Fang, C.-Y. Xia, D.-y. Kong, J.-g. Wang, H. Liu, C.-Q. Zhu, *et al.*, Highly efficient generation of 0.2 mj terahertz pulses in lithium niobate at room temperature with sub-50 fs chirped ti: sapphire laser pulses, Optics express **26**, 7107 (2018).

[15] H.-h. Huang, T. Nagashima, T. Yonezawa, Y. Matsuo, S. H. Ng, S. Juodkazis, and K. Hatanaka, Giant enhancement of thz wave emission under double-pulse excitation of thin water flow, Applied Sciences **10**, 2031 (2020).

[16] G. Liao, Y. Li, H. Liu, G. G. Scott, D. Neely, Y. Zhang, B. Zhu, Z. Zhang, C. Armstrong, E. Zemaityte, *et al.*, Multimillijoule coherent terahertz bursts from picosecond laser-irradiated metal foils, Proceedings of the National Academy of Sciences **116**, 3994 (2019).

[17] D. Nicoletti and A. Cavalleri, Nonlinear light–matter interaction at terahertz frequencies, Advances in Optics and Photonics **8**, 401 (2016).

[18] H. Hirori, K. Shinokita, M. Shirai, S. Tani, Y. Kadoya, and K. Tanaka, Extraordinary carrier multiplication gated by a picosecond electric field pulse, Nature communications **2**, 1 (2011).

[19] S. L. Lange, N. K. Noori, T. M. B. Kristensen, K. Steenberg, and P. U. Jepsen, Ultrafast thz-driven electron emission from metal metasurfaces, Journal of Applied Physics **128**, 070901 (2020).

[20] M. T. Hibberd, A. L. Healy, D. S. Lake, V. Georgiadis, E. J. Smith, O. J. Finlay, T. H. Pacey, J. K. Jones, Y. Saveliev, D. A. Walsh, *et al.*, Acceleration of relativistic beams using laser-generated terahertz pulses, Nature Photonics **14**, 755 (2020).

[21] E. A. Nanni, W. R. Huang, K.-H. Hong, K. Ravi, A. Fallahi, G. Moriena, R. D. Miller, and F. X. Kärtner, Terahertz-driven linear electron acceleration, Nature communications **6**, 1 (2015).

[22] D. Rohrbach, Z. Ollmann, M. Hayati, C. Schroeder, W. Leemans, and T. Feurer, Thz-driven split ring resonator undulator, Physical review accelerators and beams **24**, 010703 (2021).

[23] D. Zhang, A. Fallahi, M. Hemmer, H. Ye, M. Fakhari, Y. Hua, H. Cankaya, A.-L. Calendron, L. E. Zapata, N. H. Matlis, *et al.*, Femtosecond phase control in high-field terahertz-driven ultrafast electron sources, Optica **6**, 872 (2019).

[24] S. A. Ponomarenko and G. P. Agrawal, Phase-space quality factor for ultrashort pulsed beams, Optics letters **33**, 767 (2008).

[25] M. Shalaby and C. P. Hauri, Demonstration of a low-frequency three-dimensional terahertz bullet with ex-

treme brightness, Nature communications **6**, 1 (2015).
[26] Q. Lin, J. Zheng, J. Dai, I.-C. Ho, and X.-C. Zhang, Intrinsic chirp of single-cycle pulses, Phys. Rev. A **81**, 043821 (2010).
[27] C. Ruchert, C. Vicario, and C. P. Hauri, Spatiotemporal focusing dynamics of intense supercontinuum thz pulses, Phys. Rev. Lett. **110**, 123902 (2013).
[28] C. F. R. Caron and R. M. Potvliege, Free-space propagation of ultrashort pulses: Space-time couplings in gaussian pulse beams, Journal of Modern Optics **46**, 1881 (1999), https://doi.org/10.1080/09500349908231378.
[29] C. Vicario, B. Monoszlai, and C. P. Hauri, Gv/m single-cycle terahertz fields from a laser-driven large-size partitioned organic crystal, Physical review letters **112**, 213901 (2014).
[30] T. Oh, Y. Yoo, Y. You, and K. Kim, Generation of strong terahertz fields exceeding 8 mv/cm at 1 khz and real-time beam profiling, Applied Physics Letters **105**, 041103 (2014).
[31] Q. Wu, T. Hewitt, and X.-C. Zhang, Two-dimensional electro-optic imaging of thz beams, Applied Physics Letters **69**, 1026 (1996).
[32] K. Kim, B. Yellampalle, G. Rodriguez, R. Averitt, A. Taylor, and J. Glownia, Single-shot, interferometric, high-resolution, terahertz field diagnostic, Applied physics letters **88**, 041123 (2006).
[33] Z. Jiang and X.-C. Zhang, Single-shot spatiotemporal terahertz field imaging, Opt. Lett. **23**, 1114 (1998).
[34] P. A. Chizhov, A. A. Ushakov, V. V. Bukin, and S. V. Garnov, Measurement of spatio-temporal field distribution of thz pulses in electro-optic crystal by interferometry method, Quantum Electronics **45**, 434 (2015).
[35] Q. Wu and X.-C. Zhang, 7 terahertz broadband gap electro-optic sensor, Applied Physics Letters **70**, 1784 (1997).
[36] S. Casalbuoni, H. Schlarb, B. Schmidt, P. Schmüser, B. Steffen, and A. Winter, Numerical studies on the electro-optic detection of femtosecond electron bunches, Phys. Rev. ST Accel. Beams **11**, 072802 (2008).
[37] D. Zhang, A. Fallahi, M. Hemmer, X. Wu, M. Fakhari, Y. Hua, H. Cankaya, A.-L. Calendron, L. E. Zapata, N. H. Matlis, and F. X. Kärtner, Segmented terahertz electron accelerator and manipulator (steam), Nature photonics **12**, 336 (2018).
[38] P. Sprangle, E. Esarey, and A. Ting, Nonlinear theory of intense laser-plasma interactions, Phys. Rev. Lett. **64**, 2011 (1990).
[39] B. Rau, T. Tajima, and H. Hojo, Coherent electron acceleration by subcycle laser pulses, Phys. Rev. Lett. **78**, 3310 (1997).
[40] T. Arber, K. Bennett, C. Brady, A. Lawrence-Douglas, M. Ramsay, N. Sircombe, P. Gillies, R. Evans, H. Schmitz, A. Bell, and C. Ridgers, Contemporary particle-in-cell approach to laser-plasma modelling, Plasma Physics and Controlled Fusion **57**, 113001 (2015).
[41] `http://energy.gov/downloads/doe-public-access-plan`, accessed: 2021-08-04.